

# Journal of Materials Chemistry A

Accepted Manuscript

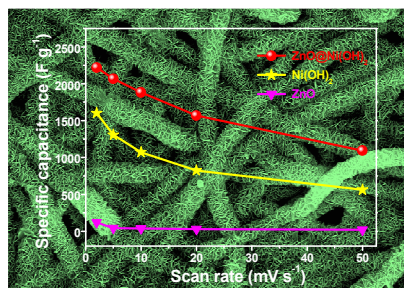


This is an *Accepted Manuscript*, which has been through the Royal Society of Chemistry peer review process and has been accepted for publication.

*Accepted Manuscripts* are published online shortly after acceptance, before technical editing, formatting and proof reading. Using this free service, authors can make their results available to the community, in citable form, before we publish the edited article. We will replace this *Accepted Manuscript* with the edited and formatted *Advance Article* as soon as it is available.

You can find more information about *Accepted Manuscripts* in the [Information for Authors](#).

Please note that technical editing may introduce minor changes to the text and/or graphics, which may alter content. The journal's standard [Terms & Conditions](#) and the [Ethical guidelines](#) still apply. In no event shall the Royal Society of Chemistry be held responsible for any errors or omissions in this *Accepted Manuscript* or any consequences arising from the use of any information it contains.



**Three-dimensional hierarchical ZnO nanofiber@Ni(OH)<sub>2</sub> nanoflake core-shell heterostructures** are fabricated by an electrospinning method combined with hydrothermal approach and exhibit outstanding electrochemical performance.

# Towards three-dimensional hierarchical ZnO nanofiber@Ni(OH)<sub>2</sub> nanoflake core-shell heterostructures for high-performance asymmetric supercapacitors

Hao Niu, Dan Zhou, Xue Yang, Xin Li, Qian Wang\*, Fengyu Qu\*

*Key Laboratory of Design and Synthesis of Functional Materials and Green Catalysis, College of Chemistry and Chemical Engineering, Harbin Normal University, Harbin 150025, China*

Design and synthesis of unique core-shell heterostructures for high-performance supercapacitors have exerted a tremendous fascination and have recently attracted intensive attention. In this paper, a three-dimensional ZnO@Ni(OH)<sub>2</sub> core-shell heterostructure is controllably synthesized through an electrospinning method combined with a hydrothermal approach. The as-prepared ZnO@Ni(OH)<sub>2</sub> heterostructures are investigated as the electrodes for supercapacitors, which exhibit excellent electrochemical performances such as ultrahigh specific capacitance (2218 F g<sup>-1</sup> at 2 mV s<sup>-1</sup>) and superior rate capability even at a high scan rate. Moreover, the assembled asymmetric supercapacitor with the as-obtained ZnO@Ni(OH)<sub>2</sub> hybrid as the positive electrode and the porous carbon microfibers as the negative electrode yields a high energy density of 57.6 Wh kg<sup>-1</sup> with the power density of 129.7 W kg<sup>-1</sup>. Hence, the ZnO@Ni(OH)<sub>2</sub> hybrid holds great promise for high-performance energy storage applications.

---

\*Corresponding authors. Tel. /fax: +86 451 88060653.

E-mail addresses: wangqianhrb@163.com (Q. Wang); qufengyuhsd@163.com (F.Y. Qu).

## 1. Introduction

With the ever-increasing environmental concerns and depleting energy sources, electrochemical storage devices for the next-generation plug-in hybrid electric vehicles and modern consumer electronics have attracted intensive attention because of their widespread applications in portable electronics, hybrid electric vehicles and so on. Of the various power source devices, supercapacitors, also known as electrochemical capacitors, with the ability of fast charging and discharging, high power density and long cycle life hold substantial promise for next-generation power devices in easing the energy crisis and meeting the urgent requirements of modern electronics industry.<sup>1</sup> Generally, carbonaceous materials,<sup>2-8</sup> metal oxides/hydroxides,<sup>9,10</sup> and conducting polymers are commonly used as available types of electrode materials for supercapacitors.<sup>11-13</sup> Especially, metal hydroxides such as Ni(OH)<sub>2</sub> and Co(OH)<sub>2</sub> has recently attracted tremendous interests because of their ultrahigh theoretical specific capacitance and energy density compared with carbon materials and other pseudocapacitive materials,<sup>12,14,15</sup> thus they have been considered as one of the most attractive candidates. However, the high specific capacitance and increase in energy density commonly come at the cost of lower power density, poorer rate capability and inferior cycling stability of the pseudocapacitive materials as a result of their poor electrical conductivity and the undesirable shrinking and swelling during the charge/discharge process, which have dramatically limits their wide application in high-performance energy storage devices.<sup>16</sup>

To meet the requirement of high capacitance and superior rate capability at rapid charge/discharge process to bridge the performance gap between traditional capacitors and batteries, design and construction of a novel hybrid electrode has drawn considerable attention since they can provide competitive electrochemical performances owing to the synergistic effects between the two individual components.<sup>17-22</sup> For instance, it has been demonstrated to be effective to incorporate metal oxides/hydroxides with conductive carbon materials such as graphene and carbon nanotubes, conducting polymer,<sup>23</sup> and construct core-shell structures such as Co<sub>3</sub>O<sub>4</sub>@MnO<sub>2</sub>,<sup>18</sup>

$\text{Ni(OH)}_2@\text{MnO}_2$ ,<sup>24</sup>  $\text{Ni}_3\text{S}_2@\text{Ni(OH)}_2$ ,<sup>25</sup> and  $\text{ZnO}@\text{NiO}/\text{MoO}_2$ .<sup>26</sup> Among the various available metal oxides scaffolds, ZnO turns out to be one of the most attractive functional semiconductor materials owing to their special chemical and physical properties and thus it could be utilized as efficient mechanical supports and electron conducting paths because of its good electric conductivity, high chemical stability and mechanical flexibility. Recently, ZnO with various morphologies has been introduced into hybrid electrodes for supercapacitors to achieve an enhanced electrochemical performance due to the synergistic effects between two individual components, such as  $\text{ZnO}@\text{MnO}_2$ ,<sup>27</sup>  $\text{ZnO}@\text{NiO}$ ,<sup>28</sup> and  $\text{ZnO}@\text{CoO}$ .<sup>29</sup>

Herein, we constructed a novel three-dimensional (3D) hierarchical  $\text{ZnO}@\text{Ni(OH)}_2$  core-shell heterostructures as the electrodes for high-performance electrochemical energy-storage application through an electrospinning method combined with a hydrothermal approach, where the ZnO nanofibers act as the well conductive “core” and ultrathin  $\text{Ni(OH)}_2$  nanoflakes are designed as the highly capacitive “shell”. This smart hybrid design offers several appealing advantages as follows: Firstly, the ZnO nanofibers could provide increased surface area for loading more active materials. Secondly, the well defined single-crystalline ZnO can serve as both the backbone and conductive substrate for the growth of  $\text{Ni(OH)}_2$ . Additionally, the ultrathin  $\text{Ni(OH)}_2$  nanoflake shells significantly increase the contact area with electrolyte, facilitating the rapid diffusion and transport of ions and consequently ensuring high-energy storage capacity and excellent rate capability. As a consequence, the well-designed and fabricated hierarchical  $\text{ZnO}@\text{Ni(OH)}_2$  core-shell heterostructures display favorable electrochemical performance, such as ultrahigh specific capacitance and excellent rate capability compared with that of ZnO and  $\text{Ni(OH)}_2$  individual component. It is found that the core-shell heterostructures exhibit an ultrahigh specific capacitance of  $2218 \text{ F g}^{-1}$  at  $2 \text{ mV s}^{-1}$  in  $6 \text{ M KOH}$  aqueous electrolyte, much higher than that of pure  $\text{Ni(OH)}_2$  electrode ( $1604 \text{ F g}^{-1}$ ). Moreover, the fabricated asymmetric supercapacitor based on the  $\text{ZnO}@\text{Ni(OH)}_2$  hybrid as the positive electrode and the previously prepared porous carbon

microfibers (PCNFs)<sup>30</sup> as the negative electrode exhibits a maximum energy density of 57.6 Wh kg<sup>-1</sup> with the power density of 129.7 W kg<sup>-1</sup>, which is highly competitive with various hybrid metal oxide systems reported previously.

## 2. Experimental

### 2.1. Preparation of ZnO nanofibers

ZnO nanofibers were prepared by an electrospinning method. In a typical experiment, zinc acetate (0.72 g) and Polyvinyl pyrrolidone (0.80 g) were dissolved in 4.9 ml of N, N-dimethylformamide solvent under vigorous stirring to obtain a homogeneous precursor solution. Subsequently, the solution was loaded into a 5 mL plastic syringe equipped with an N9-gauge needle made of stainless steel. The needle was connected to a 15 kV applied voltage and the distance between the needle tip and the collector was around 15 cm. The as-electrospun nanofibers were dried at room temperature for 24 h. Finally, the ZnO nanofibers were obtained by further annealing in air atmosphere at 550 °C for 2 h with a heating rate of 5 °C min<sup>-1</sup>.

### 2.2. Preparation of ZnO@Ni(OH)<sub>2</sub> core-shell heterostructures

The growth of Ni(OH)<sub>2</sub> nanosheets on the ZnO nanofibers was achieved through a typical hydrothermal synthesis method. Briefly, the ZnO nanofibers were well dispersed into 10 mL of a mixed aqueous solution containing 2 mmol of nickel nitrate hexahydrate and 0.3 mmol of urea under constant magnetic stirring at room temperature for 60 min. Afterwards, the solution was transferred into a Teflon-lined stainless steel autoclave, which was sealed and maintained at 120 °C for 6 h and then cooled down to room temperature. Finally, the ZnO@Ni(OH)<sub>2</sub> sample was collected, rinsed several times with distilled water and dried in a vacuum oven at 80 °C over night. Pure Ni(OH)<sub>2</sub> sample was also prepared by the same experimental procedure without the presence of ZnO nanofibers for comparison.

### 2.3. Material characterization

The crystallographic structures of the materials were determined by X-ray diffraction (XRD) equipped with Cu K $\alpha$  radiation ( $\lambda = 0.15406$  nm). X-ray photoelectron spectroscopy (XPS) was characterized using a PHI 5000 ESCA X-ray photoelectron spectrometer with a monochromated Al K $\alpha$  X-ray source (1486.6 eV) to investigate the chemical structure of the materials. Fourier transform infrared spectroscopy (FT-IR) spectra of the products were recorded on a Perkin-Elmer 580B IR spectrophotometer using KBr pellets. The thermal behavior of the materials was analyzed by thermogravimetric analysis (TGA) and differential thermal analysis (DTA, TG-209) in air atmosphere. The microstructure of the samples was investigated by a field-emission scanning electron microscopy (SEM, Hitachi S-4800) and transmission electron microscopy (TEM, Tecnai F20).

### 2.4. Electrochemical measurements

The fabrication of working electrodes was carried out as follows. Briefly, the active material (75 wt.%), carbon black (20 wt.%) and polytetrafluoroethylene (5 wt.%) were mixed and dispersed in ethanol to obtain a well-dispersed slurry, which was then coated onto the nickel foam current collectors (1 cm  $\times$  1 cm) with a spatula. The mass of the electrode was 3.4 mg after the as-fabricated electrodes were dried at 100 °C for 12 h in a vacuum oven.

All the electrochemical measurements were performed on a CHI 660D electrochemical workstation at room temperature. The electrochemical studies of the individual electrode were carried out with a three-electrode system in 6 M KOH aqueous electrolyte, in which the fabricated electrodes, platinum foil and saturated calomel reference electrode (SCE) were used as the working, counter and reference electrodes, respectively. Cyclic voltammetry (CV) tests were done between 0 to 0.45 V (vs. SCE) at different scan rates. Galvanostatic charge-discharge was performed from 5 to 20 A g<sup>-1</sup> with the potential window of 0 to 0.4 V (vs. SCE) and the electrochemical impedance

spectroscopy (EIS) measurements were carried out in the frequency range from 100 kHz to 0.1 Hz at open circuit potential with an AC amplitude of 5 mV. The specific capacitance of the electrode can be calculated based on the CV curves according to the following equation:

$$C = \int IdV / \nu mV \quad (1)$$

where  $I$  is the response current density,  $V$  is the potential,  $\nu$  is the scan rate, and  $m$  is the mass of the electroactive materials in the electrodes.

The supercapacitor performance was measured using a two-electrode system that was assembled with the ZnO@Ni(OH)<sub>2</sub> hybrid as the positive electrode and the PCNFs prepared previously<sup>30</sup> as the negative electrode with the cellulose acetate membrane as the separator. The mass ratio of the negative electrode to the positive electrode was decided based on charge balance theory ( $q_+ = q_-$ ). The charge stored ( $q$ ) by each electrode depends on the following equation:

$$q = C \times \Delta V \times m \quad (2)$$

The power density ( $P$ ) and energy density ( $E$ ) of the supercapacitor cells were calculated based on the following equations:

$$E = \frac{1}{2} C \Delta V^2 \quad (3)$$

$$P = \frac{E}{t} \quad (4)$$

where  $C$  is the specific capacitance of the asymmetric supercapacitors calculated according to the CV curves based on the total weight of the electroactive materials in two electrodes,  $\Delta V$  is the voltage scan range and  $t$  is the discharge time.

## 3. Results and discussion

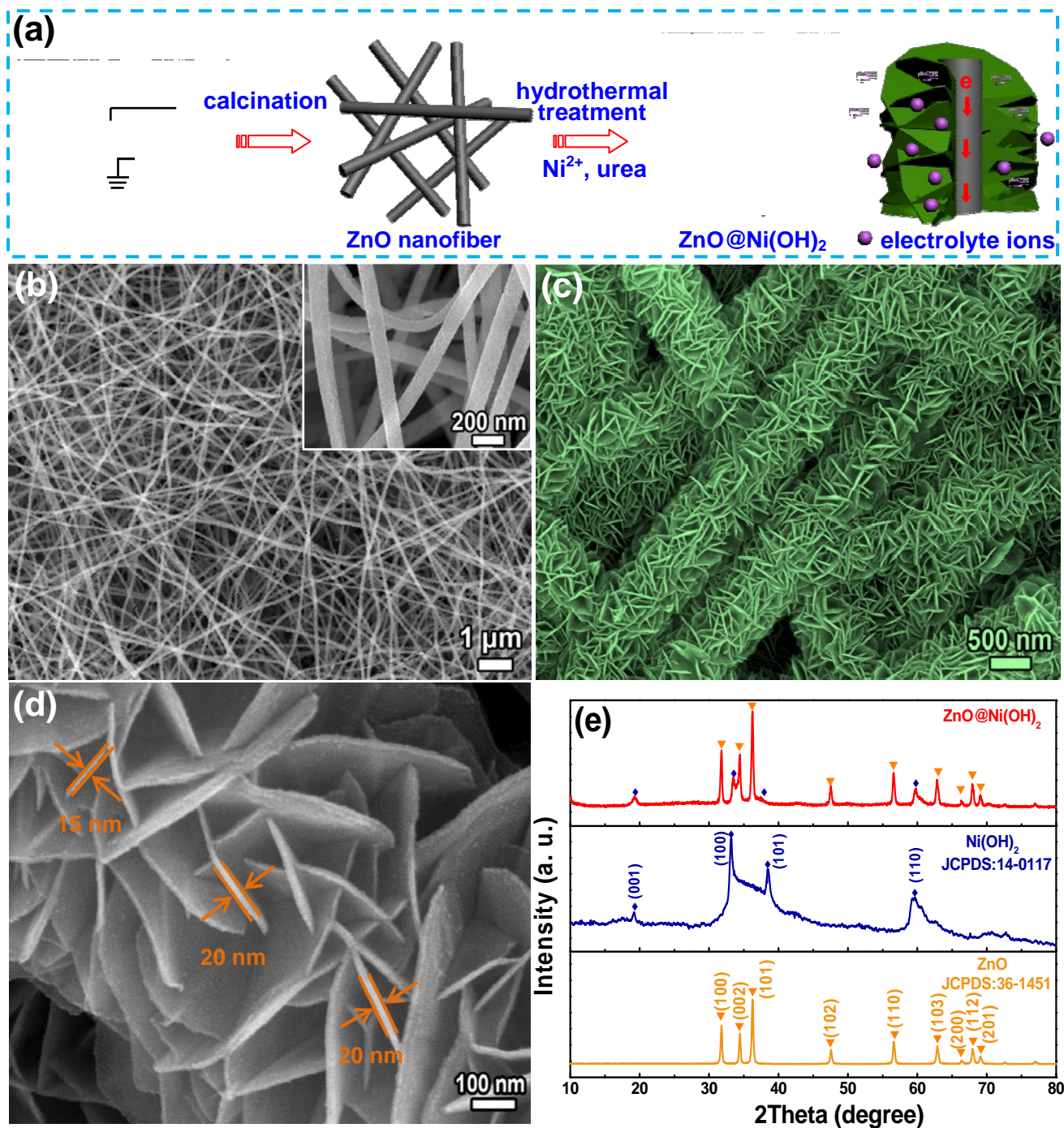


**Fig. 1** (a) Schematic illustration of the growth mechanism of the  $\text{ZnO@Ni(OH)}_2$  core-shell nanostructures. SEM images of (b) ZnO nanofibers and (c, d)  $\text{ZnO@Ni(OH)}_2$  hybrid. (e) XRD patterns of all the samples.

Fig. 1a schematically illustrates the facile synthesis process of the  $\text{ZnO@Ni(OH)}_2$  core-shell heterostructures. Typically, the ZnO nanofibers serving as the backbone for the subsequent

deposition of Ni(OH)<sub>2</sub> nanoflakes were firstly synthesized through the electrospinning process. Subsequently, ZnO@Ni(OH)<sub>2</sub> core-shell heterostructure was obtained through the growth of Ni(OH)<sub>2</sub> nanoflakes *via* a hydrothermal procedure. The Ni<sup>2+</sup> firstly reacts with OH<sup>-</sup> generated by the decomposition of urea to produce Ni(OH)<sub>2</sub> nuclei, which quickly grow into the primary particles. Then these primary particles gradually aggregate into chains that deposit on the surface of the ZnO nanofibers to become the aggregation cores of more amorphous primary particles. As the reaction progresses, the Ni(OH)<sub>2</sub> primary particles continue to aggregate. Afterwards, Ni(OH)<sub>2</sub> begins to crystallize and grows along the *c*-axis to form big nanosheets. Finally, the core-shell heterostructure is gradually formed.<sup>31,32</sup> With regard to this core-shell heterostructure as electrode materials for supercapacitors, the ZnO nanofiber core has excellent conductivity, thus could act as an excellent conductive substrate to effectively accelerate the charge transfer, guaranteeing high power capability. On the other hand, the vertical alignment of ultrathin Ni(OH)<sub>2</sub> nanoflake shells on the ZnO cores significantly increases the contact area with electrolyte ions and will facilitate the rapid ion diffusion and transport during the charge/discharge process.

To characterize the morphology and microstructures of the materials, SEM analysis are performed (Fig. 1b-d). It can be clearly observed that the ZnO substrate is composed of 3D interconnected ZnO nanofibers which have a relatively smooth surface with lengths up to several micrometers and a relatively uniform diameter of ~100 nm (Fig. 1b). The entangled network can not only facilitate the continuous transfer of electrons but also provide a large surface area for the growth of active materials, making it an ideal supporting material for the deposition of Ni(OH)<sub>2</sub>. After a facile hydrothermal process, hierarchical Ni(OH)<sub>2</sub> nanoflakes cover on almost the entire external surface of ZnO nanofibers to form compact core-shell heterostructures. The diameter of the individual hierarchical ZnO/Ni(OH)<sub>2</sub> is increased to 1 μm, much higher than those of the pristine ZnO nanofibers (Fig. 1c). High magnification SEM image (Fig. 1d) shows that the Ni(OH)<sub>2</sub> shell consists of well-defined interconnected flake-like subunits with 200-500 nm in size and 15-20 nm in

thickness, which are almost vertically grown on the surface of ZnO nanofibers. Without the guidance of ZnO nanofibers, pure Ni(OH)<sub>2</sub> possesses a morphology of flower-like architecture with 600-900 nm in diameter as shown in Fig. S1a and b. XRD measurements were carried out to characterize the phase and crystal structures and the typical XRD patterns of the as-prepared materials are shown in Fig. 1e. All the diffraction peaks of the XRD pattern for the pure ZnO can be well indexed to hexagonal phase of wurtzite-type ZnO (space group: *P63mc*, JCPDS: 36-1451) with lattice constants  $a = 3.25 \text{ \AA}$  and  $c = 5.207 \text{ \AA}$ .<sup>33</sup> For the pure Ni(OH)<sub>2</sub>, all the peaks could be ascribed to pure hexagonal structured  $\beta$ -Ni(OH)<sub>2</sub> with lattice constants  $a = 3.126 \text{ \AA}$  and  $c = 4.605 \text{ \AA}$  (JCPDS: 14-0117).<sup>34</sup> With regard to the ZnO@Ni(OH)<sub>2</sub> hybrid, three peaks occurred at  $2\theta = 19.2^\circ$ ,  $33.4^\circ$  and  $59.7^\circ$  are correspondingly assigned to the (001), (100), (101) and (110) planes of  $\beta$ -Ni(OH)<sub>2</sub>, respectively. Besides, the other diffraction peaks are in line with the standard XRD pattern of the ZnO crystal, demonstrating the successful synthesis of ZnO@Ni(OH)<sub>2</sub>.

TEM observations were performed to further confirm the unique core-shell heterostructures of ZnO@Ni(OH)<sub>2</sub> hybrid. It can be clearly observed that the nanostructures are composed of a ZnO nanofiber “core” (100 nm in diameter) and a Ni(OH)<sub>2</sub> “shell” (450 nm in thickness) and the ZnO nanofibers are uniformly covered by the ultrathin flakes, forming a typical core-shell structure (Fig. 2a), which is highly agreement with the observations from SEM images (Fig. 1c). The measured lattice spacing of 0.27 nm in the high-resolution TEM image (Fig. 2b) is corresponding to the (100) planes of Ni(OH)<sub>2</sub>. The selected-area electron diffraction (SAED) pattern taken from the edge of nanosheets shows well-defined rings (inset of Fig. 2b), indicating the polycrystalline characteristic of nickel hydroxide.<sup>25</sup> In addition, the energy dispersive X-ray spectrometry (EDS) analysis was further conducted to confirm the composition of ZnO@Ni(OH)<sub>2</sub> (Fig. 2c-h). The elemental line-scanning (Fig. 2c) elemental mappings of Ni, O, and Zn was employed to obtain the spatial distributions of the atomic contents across the ZnO@Ni(OH)<sub>2</sub> hybrid. The Zn profile exhibits a neat peak located at the center of the Ni profile, while the profile of Ni shows high intensity on both sides, directly

illustrating the core-shell configuration. Moreover, the EDS elemental mapping images further reveals that there appear a distribution of Zn, Ni and O across the structure (Fig. 2e-g), unambiguously confirming the ZnO core /Ni(OH)<sub>2</sub> shell hierarchical structure. The mapping result is in good agreement with the EDS spectrum shown in Fig. 2h, in which the Cu signal comes from Cu grid.

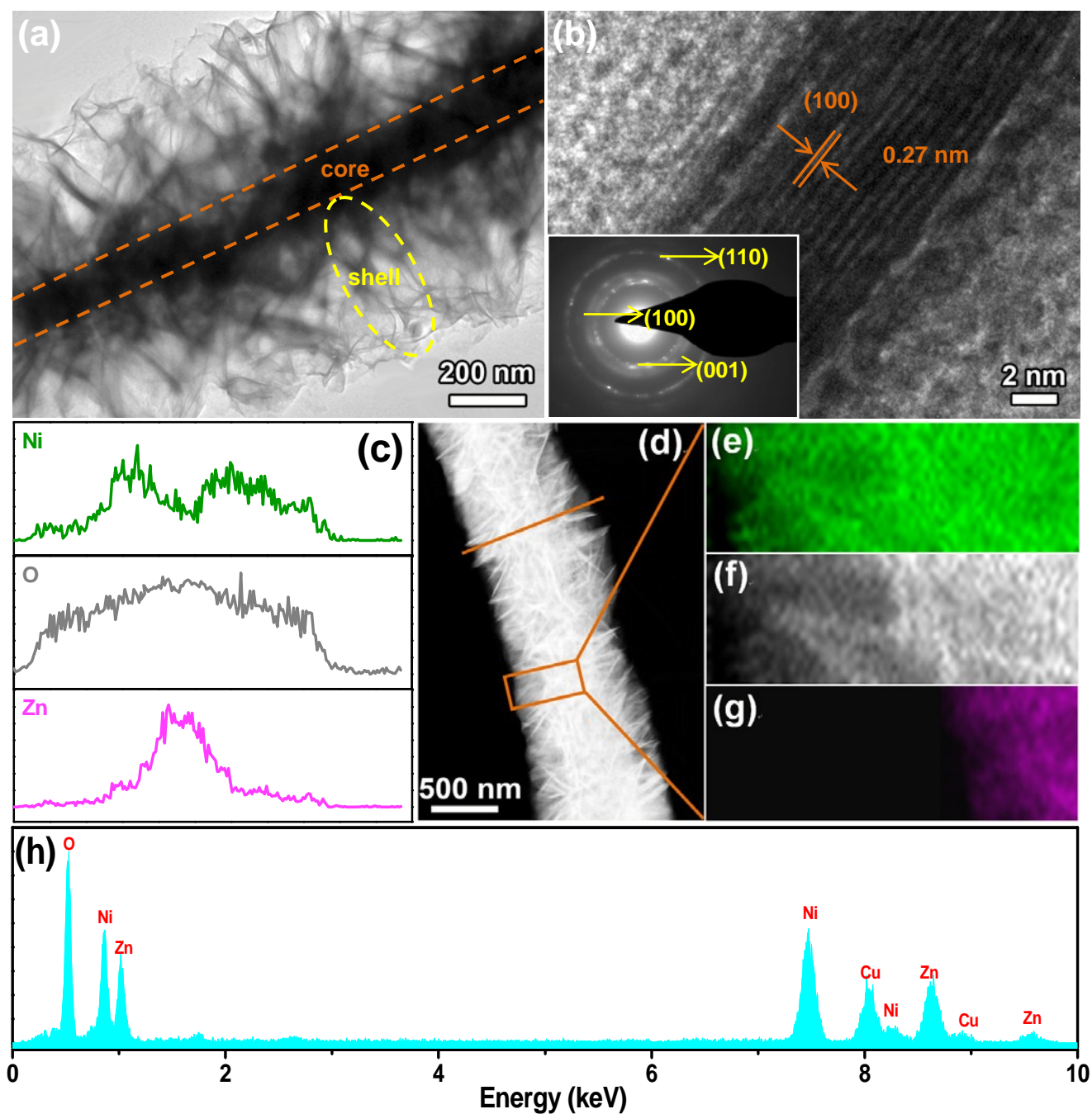


**Fig. 2** (a and b) TEM images of ZnO@Ni(OH)<sub>2</sub> core-shell nanostructures (inset of b is the corresponding SAED pattern of Ni(OH)<sub>2</sub>). (c-g) Cross sectional compositional line profiles,

elemental mapping images and (h) EDS spectrum of the hybrid.

XPS analysis confirms the presence of Zn, Ni, and O elements in the ZnO@Ni(OH)<sub>2</sub> hybrid (Fig. 3a), well consistent with the aforementioned EDS spectrum analysis results (Fig. 2h). The high-resolution XPS spectrum of Zn 2p (Fig. 3b) presents two major peaks centered at 1021.5 and 1044.5 eV with a spin-energy separation of 23 eV, corresponding to Zn 2p<sub>3/2</sub> and Zn 2p<sub>1/2</sub> levels, respectively, which is in good agreement with reported data.<sup>35,36</sup> Obviously, as for the Ni 2p spectrum, there are two shakeup satellites (indicated as “Sat”) close to spin-orbit doublets at 855.4 and 873.6 eV with a spin-energy separation of 18.2 eV, which are related to the Ni 2p<sub>3/2</sub> and Ni 2p<sub>1/2</sub> signals of Ni(OH)<sub>2</sub>, respectively (Fig. 3c).<sup>20,24,31,34,37</sup> The high-resolution spectrum for O 1s in Fig. 3d could be deconvoluted into three components.<sup>24,37</sup> Respectively, the fitting peak of O 1s at 530.8 eV is typical of the metal-oxygen bond, in comparison with the fitting peak located at 531.1 eV which is commonly associated with defects, contaminants and a number of surface species including hydroxyls, chemisorbed oxygen, under-coordinated lattice oxygen or species intrinsic to the surface of the spinel. While the peaks at 532.2 eV could be attributed to multiplicity of physi- and chemisorbed water at or near the surface. Based on the obtained XPS data, the content of Ni(OH)<sub>2</sub> in the hybrid is estimated to be 82 wt.%. Fig. S2 presents the TGA and DTA curves of the ZnO@Ni(OH)<sub>2</sub> hybrid in an air atmosphere in a temperature range from 20 to 700 °C with a heating rate of 5 °C min<sup>-1</sup>. The weight loss (3.1 wt.%) below 150 °C is assigned to the removal of the adsorbed water and the evaporation of the intercalated water molecules. Noticeably, there is a strong weight loss of 18.1 wt.% in the multistep weight loss process involving the dehydration (1.2 wt.%) and decomposition of precursors (16.9 wt.%). Thus the mass loadings of Ni(OH)<sub>2</sub> in the ZnO@Ni(OH)<sub>2</sub> hybrid could be estimated to be about 90 wt.% from the TGA curve.

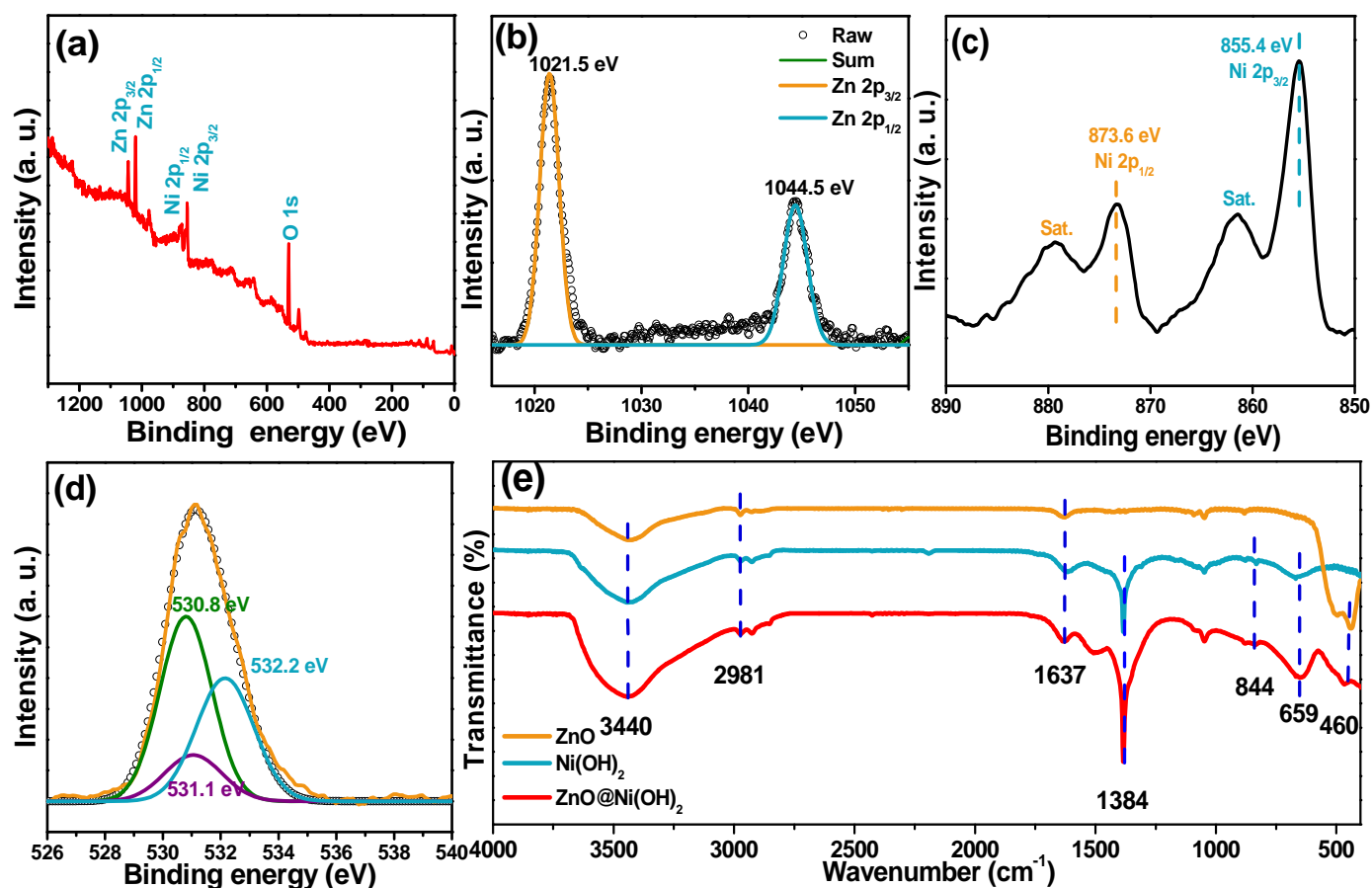


**Fig. 3** XPS spectra of (a) survey spectrum, (b) Zn 2p, (c) Ni 2p, and (d) O 1s and (e) the FT-IR spectra of as-prepared ZnO@Ni(OH)<sub>2</sub> hybrid.

FT-IR was conducted to further investigate the surface property of the hybrid (Fig. 3e). The crystal-clear band at 460 cm<sup>-1</sup> is related to the Zn-O stretching vibrations.<sup>38</sup> The weak band at 659 cm<sup>-1</sup> is corresponding to Ni-OH bending vibration, and the two bands at 1047 and 1384 cm<sup>-1</sup> are attributed to the C-N vibrations, indicating that intercalation of nitrate anions in the interlayer space.<sup>39</sup> We also confirmed that Ni(OH)<sub>2</sub> was successfully fabricated even though some intercalated nitrate and carbonate molecules are still present, which is ascribed to the open system used in the synthesis. In addition, the weak band at ~1637 cm<sup>-1</sup> indicates the bending vibration of O-H groups in the adsorbed water molecules, while the broad band centered at ~3440 cm<sup>-1</sup> corresponds to the O-H stretching vibration of the hydrogen-bonded hydroxyl groups and intercalated water molecules located in the interlamellar spaces of Ni(OH)<sub>2</sub>.<sup>40</sup>

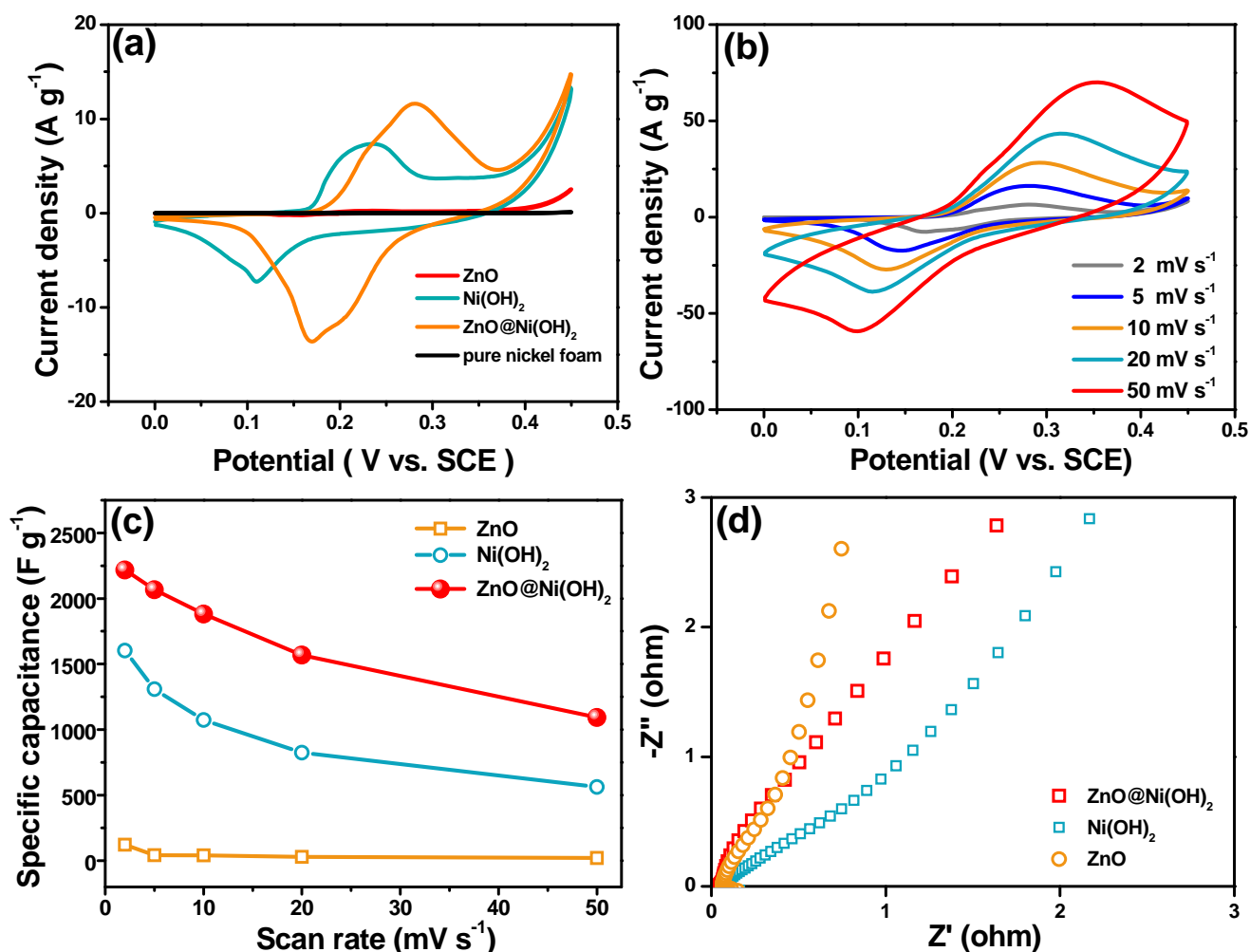
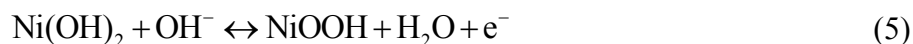


**Fig. 4** Three-electrode electrochemical measurements of the ZnO@Ni(OH)<sub>2</sub> hybrid in 6 M KOH aqueous solution: (a) CV curves of ZnO, Ni foam, Ni(OH)<sub>2</sub> and ZnO@Ni(OH)<sub>2</sub> hybrid at 2 mV s<sup>-1</sup>. (b) CV curves of the ZnO@Ni(OH)<sub>2</sub> hybrid electrode at various scan rates. (c) Average specific capacitances of the as-prepared electrodes at various scan rates. (d) Nyquist plots of the as-prepared samples.

With the aim of exploring the merits of the hybrid electrode architecture in supercapacitors, the electrochemical tests were firstly carried out in a three-electrode configuration in 6 M KOH aqueous electrolyte. Fig. 4a presents the typical CV curves of the Ni(OH)<sub>2</sub> and ZnO@Ni(OH)<sub>2</sub> hybrid electrodes at a scan rate of 2 mV s<sup>-1</sup> in the potential window ranging from 0 and 0.45 V (vs. SCE). The CV curves of pristine ZnO nanofibers and nickel foam are also shown for comparison. The shape of the CV curves of Ni(OH)<sub>2</sub> and ZnO@Ni(OH)<sub>2</sub> hybrid electrodes unambiguously

demonstrates their pseudocapacitive characteristics. Specially, a pair of well-defined redox peaks could be found for both the CV profiles of Ni(OH)<sub>2</sub> and ZnO@Ni(OH)<sub>2</sub> hybrid, distinguishable from those of electric double-layer capacitors, indicating the presence of a Faradic reaction and corresponding to the redox reaction between Ni(OH)<sub>2</sub> and NiOOH associated with OH<sup>-</sup> anions shown as follows:



In sharp contrast, no obvious redox peaks can be observed on the CV curve of ZnO electrode and it can be clearly found that the integrated area of bare nickel foam is much smaller compared with those of Ni(OH)<sub>2</sub> and ZnO@Ni(OH)<sub>2</sub> hybrid, suggesting the capacitance contribution from the Ni foam and ZnO is negligible. Notably, the integral area of the CV profile for ZnO@Ni(OH)<sub>2</sub> hybrid electrode is much higher than that of unitary ZnO and Ni(OH)<sub>2</sub> electrodes, indicating a significantly enhanced specific capacitance after the growth of Ni(OH)<sub>2</sub> nanosheets on the surface of ZnO nanofibers. The galvanostatic charge/discharge curves of all the electrodes at 5 A g<sup>-1</sup> show that the ZnO@Ni(OH)<sub>2</sub> hybrid electrode has longer discharge time, once again demonstrating a much higher specific capacitance (Fig. S3a). This result is probably due to the significant synergistic effect between ZnO supporting skeletons as a conductive core and Ni(OH)<sub>2</sub> nanosheets with high pseudocapacitance as a shell. On the one hand, ZnO has relatively good electrical conductivity and could facilitate the electron transfer during the charge/discharge process. Meanwhile, the unique porous ZnO nanofibers could increase the contact surface between active materials and electrolyte, shortening the diffusion paths of electrolyte ions. On the other hand, Ni(OH)<sub>2</sub> nanosheets can provide much higher pseudocapacitance to the overall capacitance. Fig. 4b depicts the CV curves of the ZnO@Ni(OH)<sub>2</sub> electrode at various scan rates ranging from 2 to 50 mV s<sup>-1</sup>. A distinct pair of redox peaks around 0.10 and 0.35 V (vs. SCE) can be obviously observed at all scan rates, powerfully confirming the capacitance mainly coming from pseudocapacitance. In addition, the position of the redox peaks shifts slightly with the increase of the scan rates due to the equivalent

series resistance (ESR). With the increase of scan rates, the current response increases accordingly and the shapes of CV curves are well retained, indicating an excellent rate capability. The specific capacitances calculated from the CV curves are shown in Fig. 4c. The ZnO@Ni(OH)<sub>2</sub> hybrid electrode exhibits an ultrahigh specific capacitance of 2218 F g<sup>-1</sup> at 2 mV s<sup>-1</sup>, which is much higher than that of pure Ni(OH)<sub>2</sub> (1604 F g<sup>-1</sup>) and ZnO (112 F g<sup>-1</sup>) at the same scan rate. More importantly, a high specific capacitance of 1092 F g<sup>-1</sup> can still be retained even at a scan rate of 50 mV s<sup>-1</sup>, revealing an excellent rate capability, which is highly comparable with other Ni(OH)<sub>2</sub> electrodes reported previously (Table S1). Fig. S3 presents the typical galvanostatic charge/discharge curves of the ZnO@Ni(OH)<sub>2</sub> hybrid electrode at different current densities within the potential window of 0-0.4 V (vs. SCE). Compared with pure ZnO and Ni(OH)<sub>2</sub>, The ZnO@Ni(OH)<sub>2</sub> hybrid shows much longer discharge time (Fig. S3a), indicating the highest specific capacitance. which is in good agreement with the CV curves. In addition, the ZnO@Ni(OH)<sub>2</sub> hybrid possess the smallest IR drop (0.02 V), indicating fast transfer of electrons and transport of electrolyte ions. Moreover, the charge/discharge curves of the ZnO@Ni(OH)<sub>2</sub> hybrid at different current densities exhibit deviation from the typical triangular shape of EDLCs, revealing the Faradic characteristics of the charge storage (Fig. S3b). The shoulders in the charge/discharge curves around 0.25 V (vs. SCE) during charging and 0.15 V (vs. SCE) during discharging indicate the redox reactions, which are well consistent with the CV curves. Importantly, there is no obvious IR drop even at a high current density of 20 A g<sup>-1</sup>, further demonstrating that the architecture constructed by ZnO nanofibers and Ni(OH)<sub>2</sub> nanoflakes can effectively reduce the charge-transfer resistance and significantly improve the transport and collection of electrons and electrolyte ions. The maximum specific capacitance is estimated to be 2286 F g<sup>-1</sup> based on the weight of the ZnO@Ni(OH)<sub>2</sub> hybrid at current densities of 5 A g<sup>-1</sup> (Fig. S3c). Based on the TGA and DTA profiles, the mass ratio of ZnO to Ni(OH)<sub>2</sub> was 10 to 90. The specific capacitance contribution of Ni(OH)<sub>2</sub> alone could be estimated through the following equation:

$$C_{\text{Hybrid}} = C_{\text{Zn}} \times \text{Zn}\% + C_{\text{Ni}} \times \text{Ni}\% \quad (6)$$

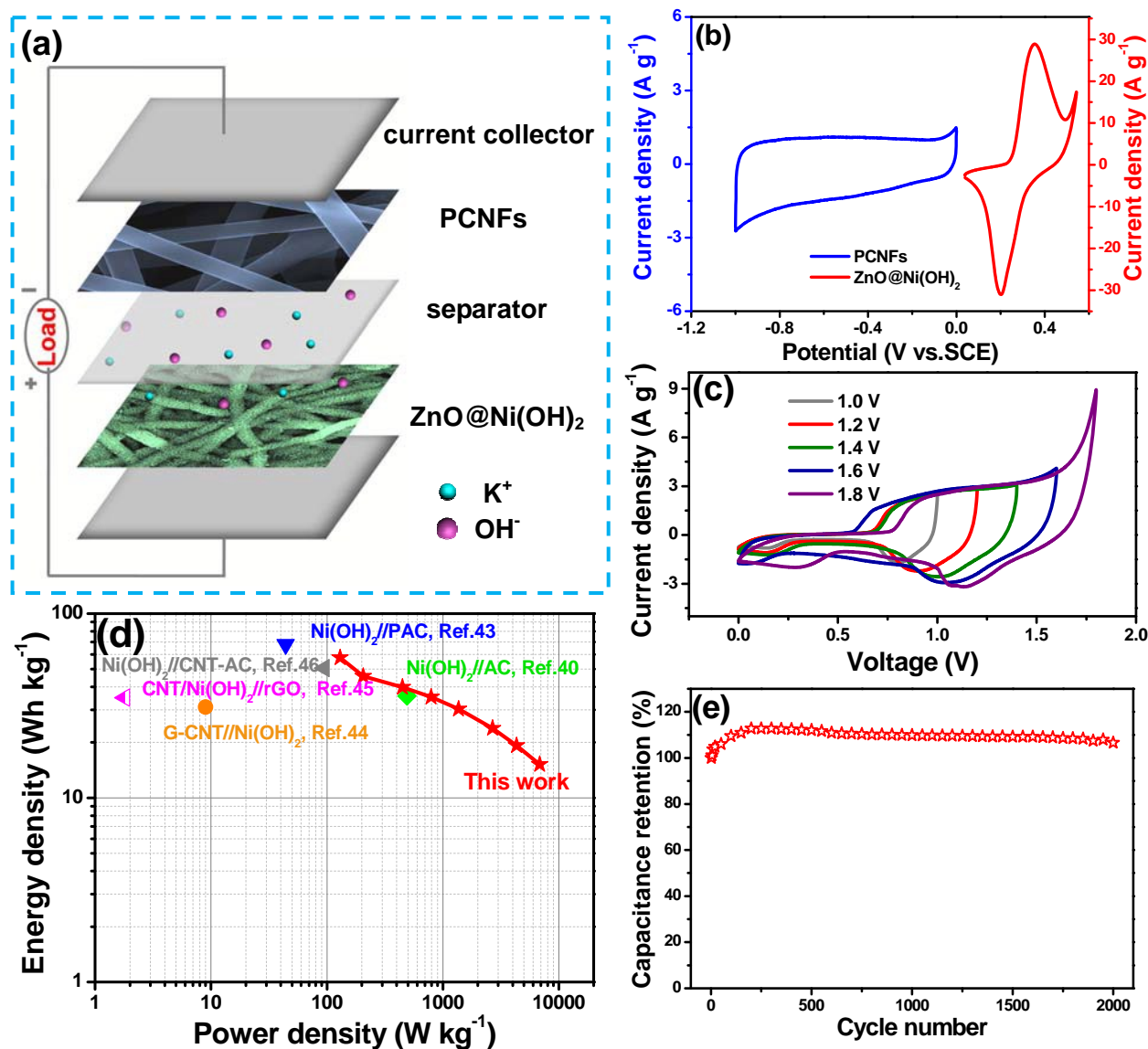


**Fig. 5** (a) Schematic illustration of the as-assembled asymmetric supercapacitor. (b) Comparative CV curves of ZnO@Ni(OH)<sub>2</sub> core-shell nanostructures and PCNF electrodes performed in a three-electrode cell in 6 M KOH aqueous solution at a scan rate of 5 mV s<sup>-1</sup>. (c) CV curves of the asymmetric supercapacitor measured at different potential windows at a scan rate of 20 mV s<sup>-1</sup>. (d) Ragone plot of the assembled ZnO@Ni(OH)<sub>2</sub>//PCNFs asymmetric supercapacitor in comparison with Ni(OH)<sub>2</sub>-based asymmetric supercapacitors reported in the literature. (e) Cycle performance of ZnO@Ni(OH)<sub>2</sub>//PCNFs asymmetric supercapacitor at 50 mV s<sup>-1</sup>.

where  $C_{\text{Ni}}$ ,  $C_{\text{Hybrid}}$ , and  $C_{\text{Zn}}$  are the specific capacitance of  $\text{Ni}(\text{OH})_2$ , the  $\text{ZnO}@\text{Ni}(\text{OH})_2$  hybrid, and pure ZnO and Zn% and Ni% are the weight percentages of ZnO and  $\text{Ni}(\text{OH})_2$  in the  $\text{ZnO}@\text{Ni}(\text{OH})_2$  composite, respectively. The specific capacitance estimated from  $\text{Ni}(\text{OH})_2$  alone was showed in Fig. S3d, which exhibits the maximum specific capacitance of  $2452 \text{ F g}^{-1}$  at  $2 \text{ mV s}^{-1}$ . The improved ions diffusion and charge transfer behavior within the electrode are also investigated using EIS measured in the frequency range from 100 kHz to 0.01 Hz at open circuit potential with an AC amplitude of 5 mV. There is no distinct semi-circle for the Nyquist plot of  $\text{ZnO}@\text{Ni}(\text{OH})_2$  hybrid electrode (Fig. 4d), suggesting small charge transfer resistance attributed to the excellent electrical conductivity of ZnO nanofiber cores. Noticeably, compared with that of  $\text{Ni}(\text{OH})_2$  electrode, the Nyquist plot of  $\text{ZnO}@\text{Ni}(\text{OH})_2$  hybrid electrode show a much higher phase angle value in the low-frequency region, indicating an ideal capacitive behavior with fast ion diffusion due to porous structure of the ZnO skeletons favorable for the rapid transport of electrolyte ions.<sup>41</sup>

Designing an asymmetric supercapacitor full cell setup have been proved to be an effective alternative approach to enhance the energy density to meet the urgent requirement of high energy density devices in practical applications. To further evaluate the possibility of using the  $\text{ZnO}@\text{Ni}(\text{OH})_2$  hybrid to construct practical supercapacitor device, an asymmetric supercapacitor was fabricated with  $\text{ZnO}@\text{Ni}(\text{OH})_2$  hybrid as the positive electrode and PCNFs as the negative electrode in 6 M KOH as electrolyte (Fig. 5a). Fig S4a shows the SEM image of the prepared PCNFs. It can be clearly found that the PCNFs have 1D nanostructure with a uniform diameter of  $\sim 1 \mu\text{m}$  and relatively smooth surface. The TEM image indicates the presence of considerable micropores in PCNFs, which could be attributed to the decomposition of the polymer and the removal of template (inset of Fig S4a). Fig. S4b exhibits the nitrogen adsorption-desorption isotherms and the pore size distribution analyzed using density functional theory method of the sample. The Brunauer-Emmett-Teller specific surface area is calculated to be  $2092 \text{ m}^2 \text{ g}^{-1}$  according to the  $\text{N}_2$  adsorption isotherm. The PCNFs exhibit specific capacitance of  $251 \text{ F g}^{-1}$  at  $2 \text{ mV s}^{-1}$  and retain 181

$\text{F g}^{-1}$  at  $50 \text{ mV s}^{-1}$  (Fig. S4d). Based on the obtained specific capacitance of the  $\text{ZnO@Ni(OH)}_2$  and PCNFs as well as the principle of charge balance between the positive and negative electrodes (Fig. 5b), the mass ratio of PCNFs to  $\text{ZnO@Ni(OH)}_2$  was controlled at about 5.3 in the asymmetric supercapacitor.<sup>42</sup> Fig. 5c displays the CV curves of the  $\text{ZnO@Ni(OH)}_2$ //PCNF asymmetric supercapacitor device in different voltage windows at a scan rate of  $20 \text{ mV s}^{-1}$ . Taking full advantage of the different potential windows of the  $\text{ZnO@Ni(OH)}_2$  and PCNFs, as expected, the stable electrochemical window of the asymmetric supercapacitor can be extended to 1.6 V. The CV curves obtained at various scan rates from 2 to  $200 \text{ mV s}^{-1}$  demonstrate that the as-assembled asymmetric supercapacitor shows a combination of both pseudocapacitance and EDLC at a voltage ranging from 0 to 1.6 V (Fig. S5a). The corresponding specific capacitance of the asymmetric supercapacitor is calculated from the CV curves based on the total mass of the active materials of the two electrodes as shown in Fig. S5b. A high specific capacitance is achieved to be  $162.1 \text{ F g}^{-1}$  at  $2 \text{ mV s}^{-1}$ . The power density and energy density are generally used as important parameters to characterize the performance of asymmetric supercapacitor devices. Fig. 5d gives the Ragone plot of the fabricated asymmetric supercapacitor for energy and power densities. The asymmetric supercapacitor achieves a high energy density up to  $57.6 \text{ Wh kg}^{-1}$  at an average power density of  $129.7 \text{ W kg}^{-1}$  and a high energy density of  $30.4 \text{ Wh kg}^{-1}$  can be retained at a power density of  $1366.4 \text{ W kg}^{-1}$ , again confirming the excellent rate performance of our fabricated  $\text{ZnO@Ni(OH)}_2$ //PCNF asymmetric device. The maximum energy density is highly comparable with those  $\text{Ni(OH)}_2$  based asymmetric supercapacitors reported previously in aqueous electrolytes, such as  $\text{Ni(OH)}_2$ //AC ( $35.7 \text{ Wh kg}^{-1}$ ),<sup>40</sup>  $\text{Ni(OH)}_2$ //PAC ( $68 \text{ Wh kg}^{-1}$ ),<sup>43</sup> G-CNT/ $\text{Ni(OH)}_2$  ( $31.1 \text{ Wh kg}^{-1}$ ),<sup>44</sup> CNT/ $\text{Ni(OH)}_2$ //rGO ( $35 \text{ Wh kg}^{-1}$ ),<sup>45</sup>  $\text{Ni(OH)}_2$ //CNT-AC ( $50.6 \text{ Wh kg}^{-1}$ )<sup>46</sup> and  $\text{ZnO@Ni(OH)}_2$  ( $54 \text{ Wh kg}^{-1}$ )<sup>47</sup> (Fig. 5d and Table S2). The high energy density should be attributed to both its high specific capacitance and its wide electrochemical window of 0-1.6 V in the aqueous electrolyte. As extended cycling life is a quite important requirement for supercapacitor applications, a cycling life test was measured by repeating

the CV test at a scan rate of  $50 \text{ mV s}^{-1}$  for 2000 cycles for the fabricated  $\text{ZnO@Ni(OH)}_2/\text{PCNF}$  asymmetric supercapacitor. Fig. 5e exhibits the capacitance retention ratio of the fabricated  $\text{ZnO@Ni(OH)}_2/\text{PCNF}$  asymmetric supercapacitor as a function of the cycle numbers. Noticeably, the slight increase of specific capacitance before 200 cycles may be attributed to the full activation process that increases the number of the available electrochemical active sites. After that, the specific capacitance gradually turns steady. Although slight degradation tendency could be observed in the following cycles, 94% of its initial capacitance can still be retained after 2000 consecutive cycles, suggesting the superior electrochemical stability and minimum damage of the asymmetric supercapacitor device. These outstanding results will make such asymmetric supercapacitor device hold substantial promise for the next-generation high-performance supercapacitors in practical applications.

The remarkable electrochemical performance of our  $\text{ZnO@Ni(OH)}_2$  hybrid electrode can be attributed to the following features: First, the porous ZnO nanofiber can serve as deposition scaffolds and provide a large surface area for the coaxial growth of  $\text{Ni(OH)}_2$  nanosheets, allowing for high mass loading of pseudocapacitive  $\text{Ni(OH)}_2$  nanosheets. Second, the ZnO cores with high electrical conductivity act as excellent conductive highways for the charge accumulation and transfer of electrons, and the porous structure provides an easy access for rapid transport of electrolyte ions, which is very critical to the high-power energy storage devices. Finally, the vertical alignment of ultrathin  $\text{Ni(OH)}_2$  nanoflake shells on the ZnO cores significantly increase the contact area between  $\text{Ni(OH)}_2$  nanoflakes and electrolyte, which effectively shortens the diffusion paths for the electrolyte ions, thus ensuring fast redox reactions and consequently improving the high electrochemical utilization of active materials.

#### 4. Conclusions

In conclusion, we have demonstrated an electrospinning method combined with a hydrothermal

approach to synthesize a hierarchical ZnO@Ni(OH)<sub>2</sub> core-shell heterostructures for high-performance supercapacitor applications. By taking full advantage of the fascinating synergistic effects between ZnO nanofiber cores and Ni(OH)<sub>2</sub> nanoflake shells, the as-prepared ZnO@Ni(OH)<sub>2</sub> hybrid electrode exhibits an ultrahigh specific capacitance of 2218 F g<sup>-1</sup> at 2 mV s<sup>-1</sup> and excellent rate capability. In addition, due to the high energy contribution of ZnO@Ni(OH)<sub>2</sub> hybrid, the fabricated asymmetric supercapacitor delivers a high energy density of 57.6 Wh kg<sup>-1</sup>, highly comparable with the previously reported Ni(OH)<sub>2</sub> based asymmetric supercapacitors. In view of the facile and cost-effective synthesis and the impressive electrochemical performance, the 3D ZnO@Ni(OH)<sub>2</sub> core-shell heterostructures might hold great promise as the potential electrode for high performance supercapacitors. Moreover, this novel strategy could also be easily extended to the design and construct of hybrid electrode with core-shell architectures for the next-generation energy storage devices.

### Acknowledgements

The authors acknowledge the financial support from the National Natural Science Foundation of China (21471041, 21171045), Natural Science Foundation of Heilongjiang Province of China (ZD201214), Technology Development Pre-project of Harbin Normal University (12XYG-11).

### References

1. J. Yan, Q. Wang, T. Wei and Z. Fan, *Adv. Energy Mater.*, 2014, **4**, 1300816.
2. Q. Zhang, M. Q. Zhao, D. M. Tang, F. Li, J. Q. Huang, B. Liu, W. C. Zhu, Y. H. Zhang and F. Wei, *Angew. Chem. Int. Ed.*, 2010, **49**, 3642-3645.
3. Z. Chen, D. Zhang, X. Wang, X. Jia, F. Wei, H. Li and Y. Lu, *Adv. Mater.*, 2012, **24**, 2030-2036.

4. X. Fan, C. Yu, J. Yang, Z. Ling, C. Hu, M. Zhang and J. Qiu, *Adv. Energy Mater.*, 2014, **5**, 1401761.
5. S. Feng, W. Li, J. Wang, Y. Song, A. A. Elzatahry, Y. Xia and D. Zhao, *Nanoscale*, 2014, **6**, 14657-14661.
6. X. Zhao, Q. Zhang, C.-M. Chen, B. Zhang, S. Reiche, A. Wang, T. Zhang, R. Schlögl and D. Su, *Nano Energy*, 2012, **1**, 624-630.
7. Y.-Z. Liu, C.-M. Chen, Y.-F. Li, X.-M. Li, Q.-Q. Kong and M.-Z. Wang, *J. Mater. Chem. A*, 2014, **2**, 5730-5737.
8. H. Hu, B. Guan, B. Xia and X. W. Lou, *J. Am. Chem. Soc.*, 2015, **137**, 5590-5595.
9. L. Huang, D. Chen, Y. Ding, S. Feng, Z. L. Wang and M. Liu, *Nano Lett.*, 2013, **13**, 3135-3139.
10. S. Peng, L. Li, H. B. Wu, S. Madhavi and X. W. Lou, *Adv. Energy Mater.*, 2015, **5**, 1401172.
11. N. T. Trang, H. V. Ngoc, N. Lingappan and D. J. Kang, *Nanoscale*, 2014, **6**, 2434-2439.
12. W. Lv, D.-M. Tang, Y.-B. He, C.-H. You, Z.-Q. Shi, X.-C. Chen, C.-M. Chen, P.-X. Hou, C. Liu and Q.-H. Yang, *ACS Nano*, 2009, **3**, 3730-3736.
13. M. Yu, Y. Han, X. Cheng, L. Hu, Y. Zeng, M. Chen, F. Cheng, X. Lu and Y. Tong, *Adv. Mater.*, 2015, **27**, 3085-3097.
14. H. Wang, H. S. Casalongue, Y. Liang and H. Dai, *J. Am. Chem. Soc.*, 2010, **132**, 7472-7477.
15. J. Yan, Z. Fan, W. Sun, G. Ning, T. Wei, Q. Zhang, R. Zhang, L. Zhi and F. Wei, *Adv. Funct. Mater.*, 2012, **22**, 2632-2641.
16. H. Hu, B. Guan, B. Xia and X. W. Lou, *J. Am. Chem. Soc.*, 2015, **137**, 5590-5595.
17. D. Kong, J. Luo, Y. Wang, W. Ren, T. Yu, Y. Luo, Y. Yang and C. Cheng, *Adv. Funct. Mater.*, 2014, **24**, 3815-3826.
18. J. Liu, J. Jiang, C. Cheng, H. Li, J. Zhang, H. Gong and H. J. Fan, *Adv. Mater.*, 2011, **23**, 2076-2081.

19. M. Huang, Y. Zhang, F. Li, Z. Wang, Alamusi, N. Hu, Z. Wen and Q. Liu, *Sci. Rep.*, 2014, **4**, 4518.
20. J.-H. Zhong, A.-L. Wang, G.-R. Li, J.-W. Wang, Y.-N. Ou and Y.-X. Tong, *J. Mater. Chem.*, 2012, **22**, 5656-5665.
21. H. Xu, X. Hu, H. Yang, Y. Sun, C. Hu and Y. Huang, *Adv. Energy Mater.*, 2014, 1401761.
22. F. Rubio-Marcos, V. Calvino-Casilda, M. A. Bañares and J. F. Fernandez, *ChemCatChem*, 2013, **5**, 1431-1440.
23. X. Xia, D. Chao, Z. Fan, C. Guan, X. Cao, H. Zhang and H. J. Fan, *Nano Lett.*, 2014, **14**, 1651-1658.
24. H. Chen, S. Zhou and L. Wu, *ACS Appl. Mater. Interfaces*, 2014, **6**, 8621-8630.
25. W. Zhou, X. Cao, Z. Zeng, W. Shi, Y. Zhu, Q. Yan, H. Liu, J. Wang and H. Zhang, *Energy Environ. Sci.*, 2013, **6**, 2216-2221.
26. S. Hou, G. Zhang, W. Zeng, J. Zhu, F. Gong, F. Li and H. Duan, *ACS Appl. Mater. Interfaces*, 2014, **6**, 13564-13570.
27. X. Sun, Q. Li, Y. Lu and Y. Mao, *Chem. Commun.*, 2013, **49**, 4456-4458.
28. H. Pang, Y. Ma, G. Li, J. Chen, J. Zhang, H. Zheng and W. Du, *Dalton Trans.*, 2012, **41**, 13284-13291.
29. D. Cai, H. Huang, D. Wang, B. Liu, L. Wang, Y. Liu, Q. Li and T. Wang, *ACS Appl. Mater. Interfaces*, 2014, **6**, 15905-15912.
30. D. Zhou, Y. Dong, L. Cui, H. Lin and F. Qu, *J. Nanopart. Res.*, 2014, **16**, 1-9.
31. H. Chen, L. Hu, Y. Yan, R. Che, M. Chen and L. Wu, *Adv. Energy Mater.*, 2013, **3**, 1636-1646.
32. J. W. Lee, J. M. Ko and J.-D. Kim, *J. Phys. Chem. C*, 2011, **115**, 19445-19454.

33. D. Cai, H. Huang, D. Wang, B. Liu, L. Wang, Y. Liu, Q. Li and T. Wang, *ACS Appl. Mater. Interfaces*, 2014, **6**, 15905-15912.
34. Z. Wu, X. L. Huang, Z. L. Wang, J. J. Xu, H. G. Wang and X. B. Zhang, *Sci. Rep.*, 2014, **4**, 3669.
35. P. Yang, X. Xiao, Y. Li, Y. Ding, P. Qiang, X. Tan, W. Mai, Z. Lin, W. Wu, T. Li, H. Jin, P. Liu, J. Zhou, C. P. Wong and Z. L. Wang, *ACS Nano*, 2013, **7**, 2617-2626.
36. Y.-B. He, G.-R. Li, Z.-L. Wang, C.-Y. Su and Y.-X. Tong, *Energy Environ. Sci.*, 2011, **4**, 1288-1292.
37. J. Zhu, L. Huang, Y. Xiao, L. Shen, Q. Chen and W. Shi, *Nanoscale*, 2014, **6**, 6772-6781.
38. B. Li and H. Cao, *J. Mater. Chem.*, 2011, **21**, 3346-3349.
39. G. Duan, W. Cai, Y. Luo and F. Sun, *Adv. Funct. Mater.*, 2007, **17**, 644-650.
40. H. B. Li, M. H. Yu, F. X. Wang, P. Liu, Y. Liang, J. Xiao, C. X. Wang, Y. X. Tong and G. W. Yang, *Nat. Commun.*, 2013, **4**, 1894.
41. B. G. Choi, J. Hong, W. H. Hong, P. T. Hammond and H. Park, *ACS Nano*, 2011, **5**, 7205-7213.
42. D. Zhou, H. Lin, F. Zhang, H. Niu, L. Cui, Q. Wang and F. Qu, *Electrochim. Acta*, 2015, **161**, 427-435.
43. Y. Yang, L. Li, G. Ruan, H. Fei, C. Xiang, X. Fan and J. M. Tour, *ACS Nano*, 2014, **8**, 9622-9628.
44. Y. Xu, X. Huang, Z. Lin, X. Zhong, Y. Huang and X. Duan, *Nano Res.*, 2012, **6**, 65-76.
45. R. R. Salunkhe, J. Lin, V. Malgras, S. X. Dou, J. H. Kim and Y. Yamauchi, *Nano Energy*, 2015, **11**, 211-218.
46. Z. Tang, C.-h. Tang and H. Gong, *Adv. Funct. Mater.*, 2012, **22**, 1272-1278.

47. I. Shakir, Z. Ali, J. Bae, J. Park and D. J. Kang, *RSC Adv.*, 2014, **4**, 6324-6329.

**Figure caption**

- Fig. 1** (a) Schematic illustration of the growth mechanism of the ZnO@Ni(OH)<sub>2</sub> core-shell nanostructures. SEM images of (b) ZnO nanofibers and (c, d) ZnO@Ni(OH)<sub>2</sub> hybrid. (e) XRD patterns of all the samples.
- Fig. 2** (a and b) TEM images of ZnO@Ni(OH)<sub>2</sub> core-shell nanostructures (inset of b is the corresponding SAED pattern of Ni(OH)<sub>2</sub>). (c-g) Cross sectional compositional line profiles, elemental mapping images and (h) EDS spectrum of the hybrid.
- Fig. 3** XPS spectra of (a) survey spectrum, (b) Zn 2p, (c) Ni 2p, and (d) O 1s and (e) the FT-IR spectra of as-prepared ZnO@Ni(OH)<sub>2</sub> hybrid.
- Fig. 4** Three-electrode electrochemical measurements of the ZnO@Ni(OH)<sub>2</sub> hybrid in 6 M KOH aqueous solution: (a) CV curves of Ni foam, ZnO, Ni(OH)<sub>2</sub> and ZnO@Ni(OH)<sub>2</sub> hybrid at 2 mV s<sup>-1</sup>. (b) CV curves of the ZnO@Ni(OH)<sub>2</sub> hybrid electrode at various scan rates. (c) Average specific capacitances of the as-prepared electrodes at various scan rates. (d) Nyquist plots of the as-prepared samples.
- Fig. 5** (a) Schematic illustration of the as-assembled asymmetric supercapacitor. (b) Comparative CV curves of ZnO@Ni(OH)<sub>2</sub> core-shell nanostructures and PCNF electrodes performed in a three-electrode cell in 6 M KOH aqueous solution at a scan rate of 5 mV s<sup>-1</sup>. (c) CV curves of the asymmetric supercapacitor measured at different potential windows at a scan rate of 20 mV s<sup>-1</sup>. (d) Ragone plot of the assembled ZnO@Ni(OH)<sub>2</sub>//PCNF asymmetric supercapacitor in comparison with Ni(OH)<sub>2</sub>-based asymmetric supercapacitors reported in the literature. (e) Cycle performance of ZnO@Ni(OH)<sub>2</sub>//PCNF asymmetric supercapacitor at 50 mV s<sup>-1</sup>.